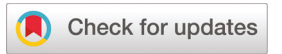
Dalton Transactions



PAPER

View Article Online
View Journal | View Issue



Cite this: *Dalton Trans.*, 2020, **49**, 2273

Received 17th October 2019, Accepted 29th January 2020 DOI: 10.1039/c9dt04069b

Synthesis, transport properties and electronic structure of p-type $Cu_{1+x}Mn_{2-x}InTe_4$ (x = 0, 0.2, 0.3)†

Dean Hobbis,^a Wencong Shi,^a Adrian Popescu,^a Kaya Wei,^{a,b} Ryan E. Baumbach,^{b,c} Hsin Wang,^d Lilia M. Woods ^a and George S. Nolas ^{*}

The synthesis, electronic structure and temperature dependent transport properties of polycrystalline $Cu_{1+x}Mn_{2-x}InTe_4$ (x=0, 0.2, 0.3) are reported for the first time. These quaternary chalcogenides were synthesized by direct reaction of the elements, followed by solid state annealing and hot press densification. The thermal conductivity is low for all specimens and intrinsic to the material system. Furthermore, the off-stoichiometry specimens illustrate the sensitivity of the transport properties to stoichiometry, with a greater than two-orders-of magnitude increase in carrier concentration with increased Cu content. First principles calculations of the electronic structure are also reported, and are in agreement with the experimental data. This fundamental investigation shows the potential towards further optimization of the electrical properties that, in addition to the intrinsically low thermal conductivity, provides a basis for further research into the viability of this material system for potential energy-related applications.

Introduction

rsc li/dalton

The search for environmentally friendly avenues for clean, renewable energy is directly related to the search for new materials with suitable structural and transport characteristics. The use of lower cost materials with primarily earthabundant constituents is especially attractive towards this end. Quaternary chalcogenides, for example with stannite and kesterite crystal structures, are one such class of materials; they have been investigated as potential new materials for both thermoelectric and photovoltaic applications.²⁻⁷ These quaternary chalcogenides typically have low thermal conductivities that may be attributed to the diverse inter-atomic distances distortion promoting scattering. 2-5,8-11 Although they possess relatively wide band gaps, a property that is of interest for photovoltaics and typically not of interest for thermoelectrics, the electrical properties can be modified by appropriate doping and/or vari-

Most recently, the transport properties of another class of quaternary chalcogenides that form in the cubic $F\bar{4}3m$ (#216) space group have been reported. These materials can be depicted as I-II₂-III-VI₄, where I = Cu or Ag; II = Cd, Zn, Ta, Co, Fe or V; III = In, Ga, Al or Tl; VI = S, Se or Te, and have been much less explored as compared to materials with the stannite or kesterite structures. In this modified zinc blende crystal structure the cations randomly distribute on the 4a (0, 0, 0) site and the Te occupy the 4c $(\frac{1}{4}, \frac{1}{4}, \frac{1}{4})$ site, as shown in Fig. 1. All of these quaternary chalcogenides are related in one aspect, the formation of stoichiometric multi-component system can be considered as a result of atomic cross substitutions accompanied by lattice mutations in which the overall valence state is preserved and the charge neutrality of a periodic crystal is maintained. All of the cubic properties of another class of the state of the cubic properties of the cubic prope

In this study we present the synthesis, first-principle electronic structure calculations and temperature dependent transport properties of $\text{Cu}_{1+x}\text{Mn}_{2-x}\text{InTe}_4$ ($x=0,\ 0.2,\ 0.3$) for the first time. A non-stoichiometric approach for doping was undertaken due to our previous findings that demonstrated dramatic changes in the transport properties with excess Cu in other quaternary chalcogenide compounds. 8,14,15,19,27 To bring more

ations in stoichiometry.^{2–5,12–15} Depending on the stoichiometry, these materials can also possess very different transport properties. For example, Cu₂ZnSnSe₄ and Ag₂ZnSnSe₄ display markedly different behavior; Cu₂ZnSnSe₄ behaves as a typical band semiconductor and Ag₂ZnSnSe₄ exhibits polaronic-type transport.^{16,17}

^aDepartment of Physics, University of South Florida, Tampa, FL, 33620, USA. E-mail: gnolas@usf.edu

^bNational High Magnetic Field Laboratory, Florida State University, Tallahassee, FL,

^cDepartment of Physics, Florida State University, Tallahassee, FL, 32306, USA

^dMaterials Science and Technology Division, Oak Ridge National Laboratory, Oak Ridge, TN, 37831. USA

[†]Electronic supplementary information (ESI) available. See DOI: 10.1039/c9dt04069b

Paper **Dalton Transactions**

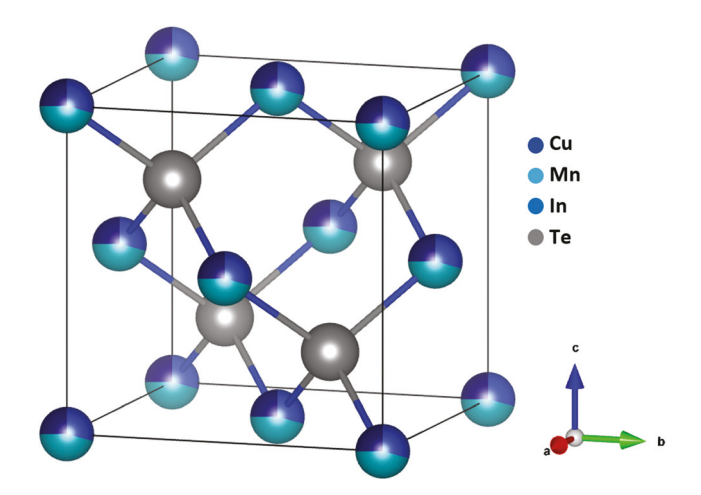


Fig. 1 Crystal structure of CuMn₂InTe₄

insight into the changes in the electronic structure, the experimental results are complemented with first-principles calculations using density functional theory (DFT). This fundamental study helps build a platform required to better understand the fundamental aspects of these materials in order to determine their suitability for use as thermoelectric, or possibly photovoltaic, materials.

Experimental and computational methods

Specimens with nominal compositions CuMn₂InTe₄, Cu_{1.2}Mn_{1.8}InTe₄ and Cu_{1.3}Mn_{1.7}InTe₄ were prepared from high purity elements, Cu powder (99.9%, Alfa Aesar), Mn powder (99.95%, Alfa Aesar), In shot (99.99%, Alfa Aesar) and Te lump (99.999+%, Alfa Aesar). The elements were loaded into silica ampoules and sealed in a quartz tube under vacuum. They were reacted in a resistive furnace at 973 K for 7 days before being quenched in air. After reaction the specimens were finely ground, cold pressed into pellets, placed in silica ampoules and sealed under vacuum in a quartz tube for annealing at 773 K for 7 days. The specimens were then ground, sieved (325 mesh) and loaded into a graphite die for hot pressing. Hot press densification was accomplished under constant N2 flow at 150 MPa and 647 K for 3 hours. The densities were obtained by measuring the specimens' dimensions and mass, with our processing resulting in polycrystalline materials with high relative densities (>95%).

Powder X-ray diffraction (XRD) data, collected in Bragg-Bretano geometry with a Bruker D8 Focus Diffractometer, a graphite monochromator and CuKα (1.54056 Å) radiation, were examined using the Rietveld method in the GSAS suite.²⁸ A JEOL JSM-6390LV Scanning Electron Microscope (SEM) equipped with an Oxford INCA X-Sight 7852 were employed for Energy Dispersive Spectroscopy (EDS). A minimum of 8 random spots across each specimen were analyzed for the EDS data. The hot-pressed pellets were cut into a 1 mm thick,

12.7 mm diameter disk for laser flash thermal diffusivity measurements, a 2 mm × 2 mm × 10 mm parallelepiped for high temperature four-probe resistivity, ρ , and Seebeck coefficient, S, measurements and a 0.5 mm \times 2 mm \times 5 mm parallelepiped for room temperature Hall measurements using a wire saw. A NETZSCH LFA457 system was used for high temperature laser flash diffusivity measurement, giving a maximum experimental uncertainty of 5%. The samples were subjected to Ar purge gas at 100 ml min⁻¹ and three measurements were repeated on each sample at each temperature set point. The ρ and S measurements were performed under -0.09 MPa static He on a ULVAC ZEM-3 system, with a maximum experimental uncertainty of 5-8%. Hall measurement data were collected at room temperature employing an AC resistive bridge four-probe technique. The specimens were subjected to a magnetic field ranging from 0.2 to 1.2 T at 0.2 T increments, where the field alternates direction at each step, in order to eliminate errors from possible miss-alignment of the voltage probes. The maximum experimental uncertainty in the Hall measurements was 13%. Magnetization measurements were carried out at low temperatures, from 1.8 to 300 K, under an applied magnetic field of 0.1 T using a Quantum Design VSM magnetic property measurement system. The heat capacity was measured from 1.8 K to 250 K using a commercial Quantum Design physical property measurement system.

Ab initio calculations based on the DFT approximation for CuMn₂InTe₄ and Cu_{1,2}Mn_{1,8}InTe₄ were performed with the projector augmented-wave (PAW) method29 as implemented in the Quantum ESPRESSO package. 30,31 The cut-off kinetic energy was set to 180 Ry. Relativistic corrections to the spinorbit coupling are also included in the calculations. For the 9 was applied, and the total energy convergence threshold was set to 10⁻⁶ eV. We use the Perdew-Zunger (LDA) exchange-correlation³² within the DFT+U method.^{33,34} The Hubbard parameter U is set to 4 eV for the Cu, Mn and In cation atoms, as suggested for Cu-based semiconductors.35 We note that our subsequent calculations indicate that the main effects from the U corrections are determined by the Mn and In atoms, while Cu plays a minor role.

Results and discussion

The structure, stoichiometry and homogeneity of the specimens were analyzed using a combination of XRD and EDS. The XRD refinement profiles are illustrated in Fig. 2, with observed and calculated patterns, and the difference between them shown. The Rietveld refinement results are shown in Table 1. All three compounds were refined in the cubic modified zinc blende crystal structure, space group F43m (#216), with the Cu/Mn/In and Te located on the 4a (0, (0, 0) and the 4c $(\frac{1}{4}, \frac{1}{4}, \frac{1}{4})$ crystallographic sites, respectively. A secondary phase, MnTe2 (Pa3, #205), was observed from our XRD data and refined to be 7% in Cu_{1.2}Mn_{1.8}InTe₄ and Cu_{1.3}Mn_{1.7}InTe₄ and 12% in CuMn₂InTe₄. The site occuDalton Transactions Paper

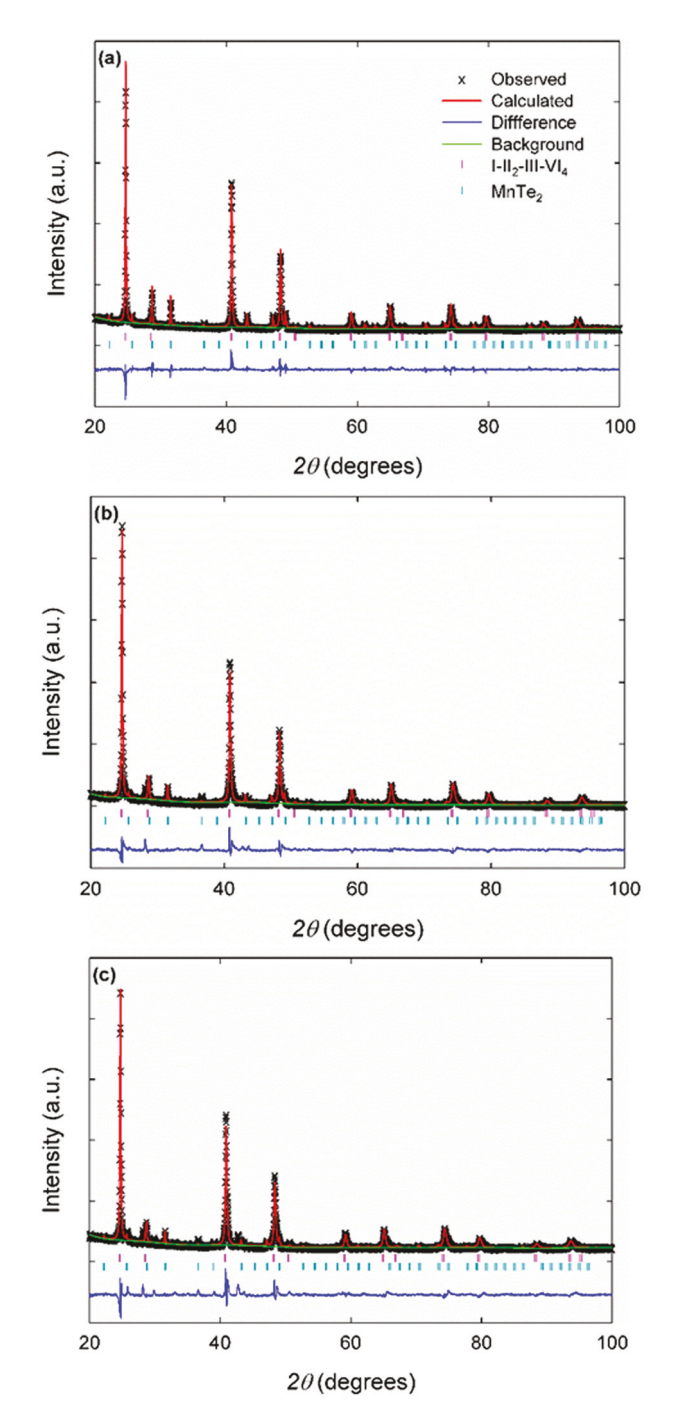


Fig. 2 Powder XRD data for (a) $CuMn_2InTe_4$, (b) $Cu_{1.2}Mn_{1.8}InTe_4$ and (c) $Cu_{1.3}Mn_{1.7}InTe_4$ including profile fit, profile difference, profile residuals and Bragg positions.

pancy for each composition indicated stoichiometries that were similar to the nominal compositions. As expected an increase in *a* with increased Cu content was observed with values of 6.2633(9) Å, 6.2653(9) Å and 6.2666(9) Å for CuMn₂InTe₄, Cu_{1.2}Mn_{1.8}InTe₄ and Cu_{1.3}Mn_{1.7}InTe₄, respectively. EDS analyses revealed good homogeneity for all three specimens with an example of the EDS elemental mapping

for Cu_{1.3}Mn_{1.7}InTe₄ shown in Fig. 3 displaying the uniform distribution of elements.

Fig. 4 shows the high-temperature thermal conductivity, κ , data and indicates κ values that are low, as in the case of other quaternary chalcogenides. $^{2-5,8-12}$ The κ values do not change significantly with stoichiometry, particularly when compared to the change in ρ (Fig. 5a), implying that lattice conductivity is dominant in these materials and the low κ values are intrinsic to this material system. As shown in Fig. 5a, the undoped specimen has very high ρ values. In comparison, the ρ values of the off-stoichiometry compounds decrease by three-ordersof magnitude relative to ρ of CuMn₂InTe₄. In addition, the temperature dependence also changes, and is more reminiscent of degenerate semiconductors in the measured temperature range. The band-gap, $E_{\rm g}$, can be estimated from the highest temperature ρ data using a fit of the form $\rho = \rho_0 \exp(E_{s}/\epsilon)$ $(2k_BT)$ where k_B is the Boltzmann constant and T is the absolute temperature. An estimated $E_{\rm g}$ value of 0.46 eV is obtained for CuMn₂InTe₄, in agreement with our theoretically calculated value, as described below. The S values shown in Fig. 5b are significantly larger for CuMn₂InTe₄ as compared with the offstoichiometry compounds, as expected given the ρ values, with S increasing with increasing temperature for the off-stoichiometry compositions up to the maximum measurement temperature. All these results indicate that the electrical properties of these materials are very sensitive to stoichiometric variations and doping.

Four-probe Hall data for CuMn₂InTe₄, Cu_{1.2}Mn_{1.8}InTe₄ and Cu_{1.3}Mn_{1.7}InTe₄ show p-type conduction with carrier concentrations, p, of 2.1×10^{17} cm⁻³, 1.8×10^{19} cm⁻³ and 2.6×10^{19} cm⁻³, respectively. These p values are in agreement with the trends for S and ρ shown in Fig. 5a and b. In addition, the Hall data corroborates the positive S values, affirming p-type conduction for all three specimens.

One can estimate the effective mass, m^* , assuming a single parabolic band model where S and p are given by 36

$$S = \pm \frac{k_{\rm B}}{e} \left(\frac{(2+r)F_{1+r}(\eta)}{(1+r)F_r(\eta)} - \eta \right) \eqno(1)$$

and

$$p = \frac{4\pi (2m_{\rm e}k_{\rm B}T)^{3/2}}{h^3} \left(\frac{m^*}{m_{\rm e}}\right)^{3/2} F_{1/2}(\eta), \eqno(2)$$

where electrons are denoted with (-) and holes are denoted with (+), e is elementary charge, η is the reduced Fermi energy given by $E_{\rm F}/k_{\rm B}T$, $m_{\rm e}$ is the mass of an electron and h is Planck's constant. F_r is the Fermi integral of order r, where r is the exponent of the energy dependence of the mean free path that takes values r=0 for scattering from acoustic phonons and r=2 for ionized impurity scattering. The intermediate value r=1 was used for our m^* estimations, resulting in, $0.2m_{\rm e}$, $0.3m_{\rm e}$ and $0.3m_{\rm e}$, for CuMn₂InTe₄, Cu_{1.2}Mn_{1.8}InTe₄ and Cu_{1.3}Mn_{1.7}InTe₄, respectively. These m^* values agree with that reported for CuZn₂InTe₄ but are considerably smaller than $1.7m_{\rm e}$ for Cu₂ZnSnSe₄. 37

Table 1 Rietveld refinement results for Cu_{1+x}Mn_{2-x}InTe₄

Nominal composition	$CuMn_2InTe_4$	$\mathrm{Cu}_{1.2}\mathrm{Mn}_{1.8}\mathrm{InTe}_4$	$Cu_{1.3}Mn_{1.7}InTe_4$
Composition	$Cu_{0.99}Mn_{1.95}In_{1.06}Te_{3.79}$	Cu _{1.13} Mn _{1.78} In _{0.98} Te _{3.94}	Cu _{1.25} Mn _{1.68} In _{1.00} Te _{3.94}
Space group, Z	$F\bar{4}3m$, (#216), 1	1110 1170 0130 0131	1120 1100 1100 0131
	6.2633(9)	6.2653(9)	6.2666(9)
a (Å) V (Å ³)	245.71(4)	245.94(9)	246.10(2)
$D_{\rm calc}$ (g cm ⁻³)	5.247	5.299	5.326
Radiation	Graphite monochromated CuK_{α} (1.54056 Å)		
Step width (°)	0.025		
WR_p, R_p	0.0780, 0.0588	0.0832, 0.0618	0.0998, 0.0711
WR_{p}, R_{p} $R(F^{2})$	0.0809	0.0663	0.0966

Atomic positions: Cu/Mn/In, 4a (0, 0, 0); Te, 4c $(\frac{1}{4}, \frac{1}{4}, \frac{1}{4})$.

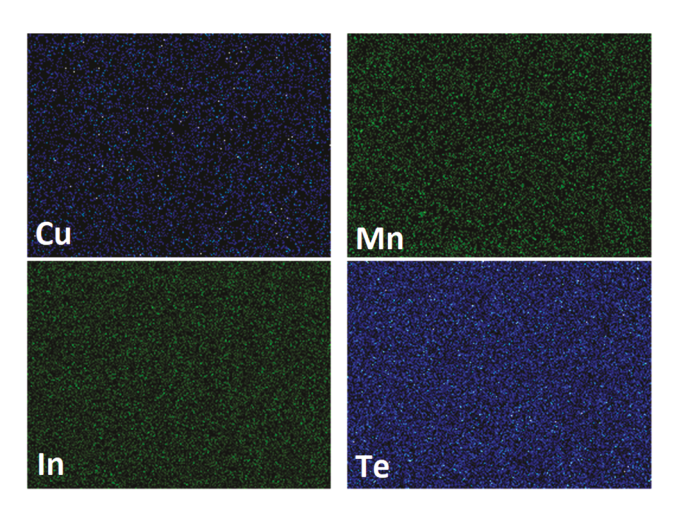


Fig. 3 EDS elemental mapping images showing Cu, Mn, In and Te, illustrating the homogeneity of $Cu_{1.3}Mn_{1.7}InTe_4$.

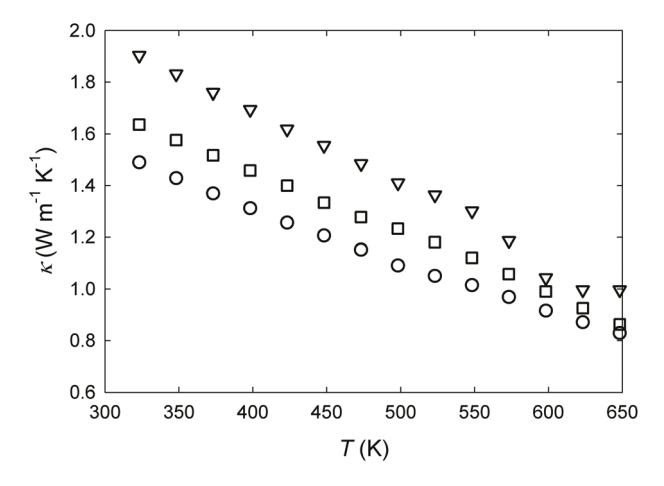


Fig. 4 Temperature dependent κ for CuMn₂InTe₄ (circle), Cu_{1.2}Mn_{1.8}InTe₄ (triangle) and Cu_{1.3}Mn_{1.7}InTe₄ (square).

To further investigate the changes in the transport properties, we perform first-principles calculations for the electronic structure of these compounds. The self-consistent calculations for both CuMn₂InTe₄ and Cu_{1,2}Mn_{1,8}InTe₄ were done at their experimentally determined lattice constants of 6.263 Å

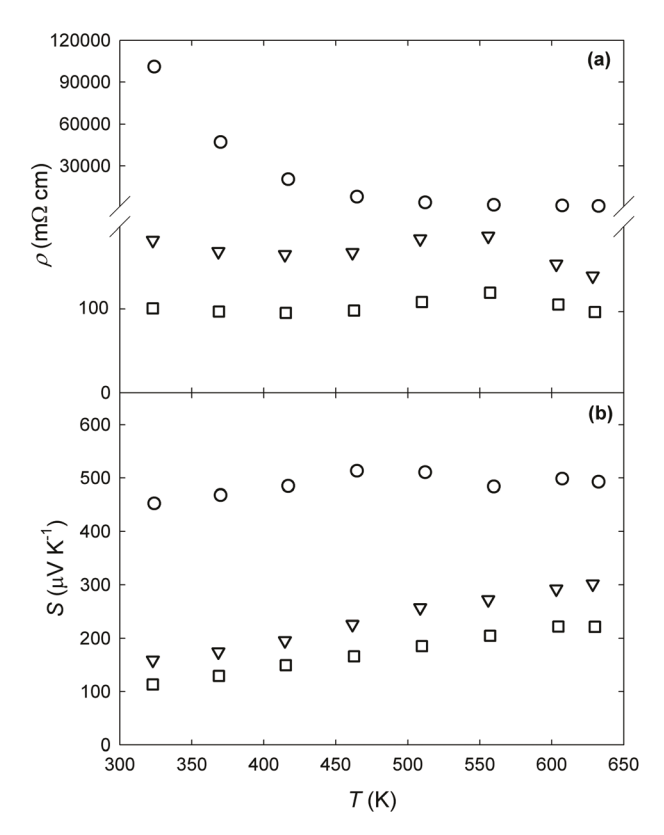


Fig. 5 Temperature dependent (a) ρ and (b) S for CuMn₂InTe₄ (circle), Cu_{1.2}Mn_{1.8}InTe₄ (triangle) and Cu_{1.3}Mn_{1.7}InTe₄ (square).

and 6.265 Å, respectively, and the $CuMn_2InTe_4$ structure is modelled on the cubic $F\bar{4}3m$ (#216) space group symmetry. For the case of $Cu_{1.2}Mn_{1.8}InTe_4$ a supercell of five $CuMn_2InTe_4$ formula units, for a total of 40 atoms, was used with one Mn atom on site 4a substituted by a Cu atom. The calculated total and spin-polarized density of states (DOS) for $CuMn_2InTe_4$ and $Cu_{1.2}Mn_{1.8}InTe_4$ are given in Fig. 6, which also shows the projected DOS on atomic species and orbitals. As seen from the figure, $CuMn_2InTe_4$ exhibits a semiconducting character with a band gap of about 0.5 eV that is in excellent agreement with our experimental data. The position of the Fermi level, E_F , right above the valence band maximum indicates that this is a p-type semiconductor, in agreement with the experimental

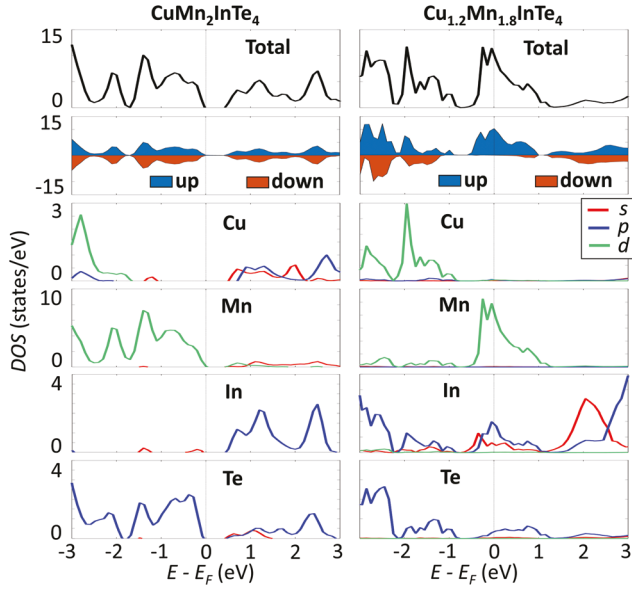


Fig. 6 Total, spin-polarized, atomic and orbital projected density of states for $CuMn_2InTe_4$ and $Cu_{1,2}Mn_{1,8}InTe_4$.

data. The projected DOS shows that the valence band has contributions predominantly from the Mn 3d orbitals, while the conduction band carries a mix of Cu 3d, In 5p, and Te 5p contributions. For the case of Cu_{1,2}Mn_{1,8}InTe₄ Fig. 6 further shows that $E_{\rm F}$ has shifted deeper in the valence range. In fact, the projected DOS indicates that the majority of the contribution at $E_{\rm F}$ comes from the Mn 3d levels with some admixture of the In 5p and Te 5p orbitals. The DOS obtained from the spin-polarized calculations indicates that while CuMn₂InTe₄ shows a spinunpolarised character, with negligible differences between the majority and minorities spins, the Cu_{1.2}Mn_{1.8}InTe₄ exhibits a sizeable spin-gap at $E_{\rm F}$ for the minority spins suggesting a ferromagnetic-like behaviour. We also find that doping does not affect m^* , which has also been observed in Mn-containing stannite quaternary chalcogenides.³⁸ The calculated total DOS at the Fermi level is 11 states eV^{-1} .

The characteristic behavior of the relatively large resistivity and Seebeck coefficient in $CuMn_2InTe_4$, as well as the temperature dependence, is consistent with the semiconducting nature of this undoped material as found from our simulations. The doped $Cu_{1.2}Mn_{1.8}InTe_4$ compound, on the other hand, exhibits transport behavior like that of degenerate semiconductors. This is corroborated by the fact that ρ is several orders of magnitude smaller than ρ for $CuMn_2InTe_4$ and S increases with temperature (Fig. 5). These metallic-like characteristics are consistent with the large S and small κ (Fig. 4 and 5), which are typical for semiconductors. The calculated DOS is in agreement with the metallic-like electronic nature of the transport in the doped material.

Fig. 7(a) shows the temperature dependent magnetization of $\text{Cu}_{1.2}\text{Mn}_{1.8}\text{InTe}_4$. At higher temperatures, $1/\chi(T)$ is in good agreement with the Curie–Weiss law with an effective magnetic moment of $5.9\mu_{\text{B}}/\text{Mn}$. This value indicates a 2+ valence state for

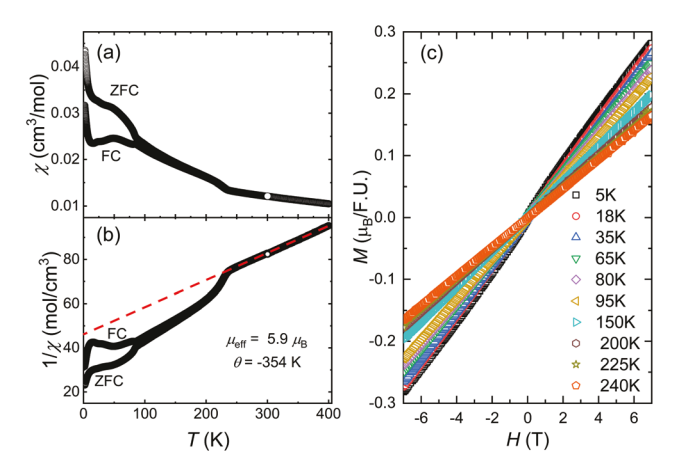


Fig. 7 (a) The magnetic susceptibility and (b) the inverse magnetic susceptibility, $\chi^{-1} = H/M$, vs. temperature for H = 0.1 T. The dashed line is the Curie–Weiss fit to the higher temperature data. (c) Magnetization field dependence at different temperature.

Mn. The large negative value of the Curie–Weiss constant (θ) , -354 K, suggests strong magnetic interaction between the itinerant Mn 3d electrons, in agreement with our spin-polarized DOS calculations. A ferromagnetic-like phase transition appears near 250 K. The field dependent magnetization curves are summarized in Fig. 7(c). M(H) is non-saturating up to 7 T where hysteretic s-shaped curves suggest a hint of ferromagnetic ordering at low temperatures. However, no magnetic transition was observed from our heat capacity, C_p , measurements, as shown in Fig. 8; therefore, free spin re-orientation or domain boundary evolution may be the main contributions to the changes of the $1/\chi(T)$ at low temperatures. Measurements on single-crystals would be needed in order to completely reveal the anisotropy of the magnetic ordering along different orientations.

Fig. 8 shows $C_{\rm p}$ of Cu_{1.2}Mn_{1.8}InTe₄ as a function of temperature, where the inset of Fig. 8 shows the $C_{\rm p}/T=\gamma+\beta T^2$ relation at low temperatures. Here γ is the Sommerfeld coeffi-

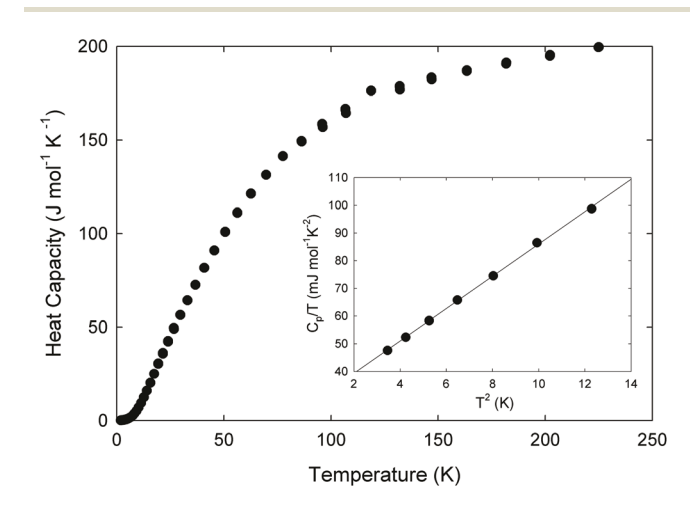


Fig. 8 Temperature dependent $C_{\rm p}$ of Cu_{1.2}Mn_{1.8}InTe₄. The inset shows $C_{\rm p}/T$ vs. T^2 data at low temperatures with the solid line representing the $C_{\rm p}/T=\gamma+\beta T^2$ relation.

Paper **Dalton Transactions**

cient of the electronic contribution and β is the coefficient of the lattice contribution.^{39,40} From this fit we obtain $\gamma = 31$ mJ $\text{mol}^{-1} \text{ K}^{-2}$ and $\beta = 5.9 \text{ mJ mol}^{-1} \text{ K}^{-4}$. Using the relation

$$\theta_{\rm D} = \left(\frac{12\pi^4 R n_{\rm a}}{5\beta}\right)^{1/3},\tag{3}$$

where $\theta_{\rm D}$ is the Debye temperature, R is the molar gas constant and n_a is the number of atoms per formula unit. The best fit to the low temperature data gives a value for the effective θ_D to be 138 K. We can also estimate the density of states at the Fermi level, $N(E_{\rm F})$, using the relation

$$\gamma = \frac{\pi^2 k_{\rm B}^2}{3} N(E_{\rm F}) (1 + \lambda_{\rm e-ph}), \tag{4}$$

where λ_{e-ph} is the electron-phonon coupling factor. Setting $\lambda_{\rm e-ph}$ to zero as a first approximation, we obtain $N(E_{\rm F})=13$ states eV⁻¹ per formula unit, in good agreement our theoretical computations described above.

Conclusions

The synthesis, crystal and electronic structure, and high temperature transport properties of CuMn₂InTe₄ have been reported for the first time. Off-stoichiometric specimens resulted in an increase in p with increasing Cu content. The κ values are low for all three compositions, and a two orders-of-magnitude reduction in ρ with excess Cu was observed as compared to that of CuMn₂InTe₄. The possibility of varying the carrier concentration substantially with excess Cu, without employing doping with another element, indicates that greater control of the carrier concentration is potentially possible in this material system, thus presumably allowing for further optimization of the thermoelectric properties. In fact, we find that while the undoped material behaves as a semiconductor, the transport of the doped compositions is consistent with that of degenerate semiconductors. The ab initio calculations also confirm our experimental results; the calculated value for the total DOS agrees well with that obtained from our Cp data. Although the ZT values for these materials is low, 41 ZT $(S^2T/\rho\kappa) = 0.04$ for the off-stoichiometric compositions at the highest measured temperature, the fact that κ is intrinsically low in addition to the ability to vary the electrical properties substantially with composition indicates that doping studies may result in much improved thermoelectric performance at higher temperatures.

Conflicts of interest

There are no conflicts to declare.

Acknowledgements

The authors acknowledge financial support from the U.S. National Science Foundation (NSF) under Grant

DMR-1748188. D. H. acknowledges support from the II-VI Foundation Block-Gift program. K. W. acknowledges the support of the Jack E. Crow Postdoctoral Fellowship. A portion of this work was performed at the National High Magnetic Field Laboratory, which is supported by the National Science Foundation Cooperative Agreement No. DMR-1644779 and the State of Florida. H. W. acknowledges support of the International Energy Agency (IEA) Advanced Materials For Transportation and the Department of Energy Lightweight and Propulsion Materials program under the Vehicle Technologies Office. Oak Ridge National Laboratory is managed by UT-Battelle LLC under contract DE-AC05000OR22725. The use of University of South Florida Research Computing Facilities is acknowledged. The authors also Dr A. R. Khabibullin for his assistance with this paper.

Notes and references

- 1 C. Rae and F. Bradley, Renewable Sustainable Energy Rev., 2012, 16, 6497.
- 2 X. Y. Shi, F. Q. Huang, M. L. Liu and L. D. Chen, Appl. Phys. Lett., 2009, 94, 122103.
- 3 M. L. Liu, I. W. Chen, F. Q. Huang and L. D. Chen, Adv. Mater., 2009, 21, 3808.
- 4 M. Ibanez, D. Cadavid, R. Zamani, N. Garcia-Castello, V. Izquierdo-Roca, W. Li, A. Fairbrother, J. D. Prades, A. Shavel, J. Arbiol, A. Perez-Rodriguez, J. R. Morante and A. Cabot, Chem. Mater., 2012, 24, 562.
- 5 W. G. Zeier, Y. Pei, G. Pomrehn, T. Day, N. Heinz, C. P. Heinrich, G. J. Synder and W. J. Tremel, J. Am. Chem. Soc., 2013, 135, 726.
- 6 D. Shin, B. Saparov, T. Zhu, W. P. Huhn, V. Blum and D. B. Mitzi, Chem. Mater., 2016, 28, 4771.
- 7 P. Balaz, M. Balaz, M. J. Sayagues, A. Eliyas, N. G. Kostova, M. Kanuchova, E. Dutkova and A. Zorkovska, Crystals, 2017, 7, 367.
- 8 M. L. Liu, F. Q. Huang, L. D. Chen and I. W. Chen, Appl. Phys. Lett., 2012, 94, 202103.
- 9 M. Ibanez, R. Zamani, A. Lalonde, D. Cadavid, W. Li, A. Shavel, J. Arbiol, J. R. Morante, S. Gorsse, G. J. Snyder and A. Cabot, J. Am. Chem. Soc., 2012, 134, 4060.
- 10 G. J. Snyder and E. S. Toberer, Nat. Commun., 2008, 7, 105.
- 11 D. Chen, Y. Zhao, Y. Chen, B. Wang, Y. Wang, J. Zhou and Z. Liang, ACS Appl. Mater. Interfaces, 2015, 7, 24403.
- 12 Y. Dong, H. Wang and G. S. Nolas, Phys. Status Solidi RRL, 2014, 8, 61.
- 13 Y. Dong, B. Eckert, H. Wang, X. Zeng, T. M. Tritt and G. S. Nolas, Dalton Trans., 2015, 44, 9014.
- 14 K. Wei, L. Beauchemin, H. Wang, W. D. Porter, J. Martin and G. S. Nolas, J. Alloys Compd., 2015, 650, 844.
- 15 Y. Dong, L. Wojtas, J. Martin and G. S. Nolas, J. Mater. Chem. C, 2015, 3, 10436.
- 16 K. Wei and G. S. Nolas, ACS Appl. Mater. Interfaces, 2015, 7,

Dalton Transactions Paper

- 17 K. Wei, A. R. Khabibullin, T. Stedman, L. M. Woods and G. S. Nolas, *J. Appl. Phys.*, 2017, **122**, 105109.
- 18 G. S. Nolas, S. M. Hassan, Y. Dong and J. Martin, *J. Solid State Chem.*, 2016, 242, 50.
- 19 D. Hobbis, K. Wei, H. Wang and G. S. Nolas, *J. Alloys Compd.*, 2018, 743, 543.
- 20 W. Shi, A. R. Khabibullin, D. Hobbis, G. S. Nolas and L. M. Woods, *J. Appl. Phys.*, 2019, 125, 155101.
- 21 L. Garbato and F. Ledda, Solid State Chem., 1979, 30, 189.
- 22 M. S. Hasanova and C. I. Abilov, *Int. Sci. Eng. Appl. Sci.*, 2017, 3, 145.
- 23 K. Momma and F. Izumi, *J. Appl. Crystallogr.*, 2011, 44, 1272.
- 24 L. Pauling, J. Am. Chem. Soc., 1929, 51, 1010.
- 25 C. H. L. Goodman, J. Phys. Chem. Solids, 1958, 6, 305.
- 26 B. Pamplin, J. Phys. Chem. Solids, 1964, 25, 675.
- 27 P. Qiu, X. Shi and L. Chen, Energy Storage Mater., 2016, 3, 85.
- 28 B. H. Toby, J. Appl. Crystallogr., 2001, 34, 210.
- 29 P. E. Blochl, Phys. Rev. B: Condens. Matter Mater. Phys., 1994, 50, 17953.
- 30 P. Giannozzi, et al., J. Phys.: Condens. Matter, 2017, 29, 465901.
- 31 P. Giannozzi, et al., J. Phys.: Condens. Matter, 2009, 21, 395502.

- 32 J. P. Perdew and A. Zunger, Phys. Rev. B: Condens. Matter Mater. Phys., 1981, 23, 5048.
- 33 A. I. Liechtenstein, V. I. Anisimov and J. Zaanen, *Phys. Rev. B: Condens. Matter Mater. Phys.*, 1995, 52, R5467(R).
- 34 V. I. Anisimov, J. Zaanen and O. K. Andersen, *Phys. Rev. B: Condens. Matter Mater. Phys.*, 1991, 44, 943.
- 35 Y. Zhang, L. L. Xi, Y. W. Wang, J. W. Zhang, P. H. Zhang and W. Zhang, *Comput. Mater. Sci.*, 2015, **108**, 239.
- 36 G. A. Slack and M. A. Hussain, J. Appl. Phys., 1991, 70, 2694.
- 37 Y. Zhu, Y. Liu, X. Tan, G. Ren, M. Yu, T. Hu, A. Marcelli and W. Xu, *AIP Adv.*, 2018, **8**, 045218.
- 38 Q. Song, P. Qiu, H. Chen, K. Zhao, D. Ren, Z. Shi and L. Chen, ACS Appl. Mater. Interfaces, 2018, 10, 10123.
- 39 U. Aydemir, C. Candolfi, H. Bormann, M. Baitinger, A. Ormeci, W. Carillo-Cabrera, C. Chubilleau, B. Lenoir, A. Dauscher, N. Oeschler, F. Steiglich and Y. Grin, *Dalton Trans.*, 2010, 39, 1078.
- 40 Y. Singh, Y. Lee, S. Nandi, A. Kreyssig, A. Ellern, S. Das, R. Nath, B. N. Harmon, A. I. Goldman and D. C. Johnston, *Phys. Rev. B: Condens. Matter Mater. Phys.*, 2008, 78, 104512.
- 41 G. S. Nolas, J. Sharp and H. J. Goldsmid, *Thermoelectrics:* Basic Principles and New Materials, Springer-Verlag, Berlin, 2001.